

## THREE-DIMENSIONAL SPECTRAL SIMULATIONS OF ANELASTIC TURBULENT CONVECTION

KALOYAN PENEV<sup>1</sup>, JOSEPH BARRANCO<sup>2</sup>, AND DIMITAR SASSELOV<sup>3</sup>

<sup>1</sup> Astronomy Department, Harvard University, 60 Garden St., M.S. 10, Cambridge, MA 02138, USA

<sup>2</sup> Department of Physics and Astronomy, San Francisco State University, 1600 Holloway Avenue, San Francisco, CA 94132-4163, USA

<sup>3</sup> Astronomy Department, Harvard University, 60 Garden St., M.S. 16, Cambridge, MA 02138, USA

Received 2009 July 13; accepted 2011 April 11; published 2011 June 6

### ABSTRACT

We have adapted the anelastic spectral code of Barranco & Marcus to simulate a turbulent convective layer with the intention of studying the effectiveness of turbulent eddies in dissipating external shear (e.g., tides). We derive the anelastic equations, show the time integration scheme we use to evolve these equations, and present the tests we ran to confirm that our code does what we expect. Further, we apply a perturbative approach to find an approximate scaling of the effective eddy viscosity with frequency and find that it is in general agreement with an estimate obtained by applying the same procedure to a realistic simulation of the upper layers of the solar convective zone.

*Key words:* convection – hydrodynamics – methods: analytical – turbulence

*Online-only material:* color figures

### 1. INTRODUCTION

Dissipation of stellar tides and oscillations is often considered to be mainly due to the turbulent flow in their convective zones. Usually, the effects of the turbulent flow are parameterized by some sort of effective viscosity coefficient. Clearly, the situation is not as simple as that and the usual “fix” is to allow this viscosity coefficient to depend on the perturbation being dissipated, most notably its frequency and perhaps the direction of the shear it creates.

Completely analytical treatments start by assuming a Kolmogorov spectrum for the turbulent flow and combine it with some prescription for the effectiveness of eddies in dissipating perturbations of the given period. Since Kolmogorov turbulence is isotropic, the direction of shear is unimportant in such prescriptions. Two such prescriptions have been used.

The first, proposed by Zahn (1966, 1989), states that when the period of the perturbation ( $T$ ) is shorter than the turnover times of some eddies, their dissipation efficiency should be proportional to the fraction of a churn they manage to complete in half a perturbation period. In this case the dissipation is dominated by the largest local eddies, and the effective viscosity coefficient scales like

$$\nu = \nu_{\max} \min \left[ \left( \frac{T}{2\tau} \right), 1 \right], \quad (1)$$

where  $\tau$  is the turnover time of the eddies with the largest size.

The second prescription is due to Goldreich & Nicholson (1977) and Goldreich & Keeley (1977). They argue that eddies with turnover times much greater than the period of the perturbation will not contribute appreciably to the dissipation, and hence the effective viscosity should be dominated by the largest eddies with turnover times shorter than  $T/2\pi$ . Then, the Kolmogorov prescription of turbulence predicts that the effective viscosity will scale as

$$\nu = \nu_{\max} \min \left[ \left( \frac{T}{2\pi\tau} \right)^2, 1 \right]. \quad (2)$$

Zahn’s prescription has been tested against tidal circularization times for binaries containing a giant star (Verbunt & Phinney 1995) and is in general agreement with observations. Also

Zahn’s prescription is in better agreement with observed tidal dissipation of binary stars in clusters (Meibom & Mathieu 2005) and with the location of the red edge of the Cepheid instability strip (Gonczi 1982).

The less efficient prescription has been used successfully by Goldreich & Keeley (1977), Goldreich & Kumar (1988), and Goldreich et al. (1994) to develop a theory for the damping of the solar  $p$ -modes. In this case, the more effective dissipation would require dramatic changes in the excitation mechanism in order to explain the observed amplitudes.

Finally, Goodman & Oh (1997) developed a perturbative derivation of the convective viscosity, which for a Kolmogorov scaling gives a result that is closer to the less efficient Goldreich & Nicholson viscosity than it is to Zahn’s. While providing a firmer theoretical basis for the former scaling, this does not resolve the observational problem of insufficient tidal dissipation.

The development of two-dimensional (2D) and three-dimensional (3D) simulations of solar convection hints at a possible resolution of this problem. The convective flow that these simulations predict is fundamentally very different from the assumed Kolmogorov turbulence (Sofia & Chan 1984; Stein & Nordlund 1989; Malagoli et al. 1990). The first major difference is that the frequency power spectrum of the velocity field is much flatter than the Kolmogorov power spectrum, and hence one might expect that the dissipation will decrease significantly slower as frequency increases relative to the Kolmogorov case. Another major difference is that the velocity field is no longer isotropic, and hence one would expect it to react differently to shear in different directions. That is, if we would use an effective viscosity coefficient, it should be a tensor and not a scalar quantity.

As a first step in investigating that possibility (Penev et al. 2009b), we applied the perturbative approach developed by Goodman & Oh (1997) to numerical models (Robinson et al. 2003) of small portions of the stellar convection of low-mass stars to find the scaling of the components of the effective viscosity tensor with frequency. Somewhat unexpectedly, we found that the scaling closely follows Zahn’s prescription, even though when the same approach is applied to Kolmogorov turbulence it gives results closer to those of Goldreich and collaborators.

That left a lot of questions unanswered. For example: are the effects of turbulence anything at all like that of molecular viscosity? Is taking only the lowest order term in a power series expansion of the energy dissipation rate an acceptable approximation? Is the turbulent dissipation dominated by the largest eddies as Zahn (1966) claims or are the eddies with turnover times closest to the external period the most important ones, like in the Goldreich and collaborators picture?

The perturbative approach also assumes that the spatial scale of the external shear being dissipated is large compared to all convective scales and hence can be assumed to be a linear function of position, but it would be interesting to see how quickly dissipation efficiency is lost as the spatial scale of the external shear decreases.

To tackle these questions, we adapted the anelastic spectral code of Barranco & Marcus (2006) to simulate a convectively unstable box in which we are able to place external, time-dependent shear as part of the evolution equations and observe the effects of the turbulent convective flow directly.

In order to make the code suitable to simulate convection, it was necessary to provide a mechanism that would supply energy at the bottom of the box and remove it at the top. To accommodate this, heat diffusion was added that allows heat to enter/leave through the bottom/top wall, and drive the convective motions. This, in turn, necessitated that we allow for a more general background state, slightly modified treatment of the pressure, and the introduction of boundary conditions on the temperature. In addition, we added an external forcing term and removed the Keplerian shear and the accompanying it shearing coordinates.

The resulting code is ideal for our purposes for the following reasons.

1. The anelastic approximation means no shock or sound waves can exist, and hence the time steps can be much larger than for a fully compressible code, and yet buoyancy phenomena, such as convection, can occur, unlike in completely incompressible codes. This allows us to get much closer to the actual timescales of interest (usually of order hours or days), than a fully compressible code would. The Boussinesq approximation has those same properties, however it is not suitable for simulating stratified convection, where the buoyancy does not depend only on the temperature.
2. Spectral codes are more efficient at simulating turbulent flows than finite difference codes, because their spatial accuracy is exponential rather than a power law, so they are capable of reliably reproducing the turbulent flow, even at modest resolutions.
3. The grid happens to have higher density near the top and bottom of the box, where it is needed in order to resolve the boundary layers that develop there due to the boundary conditions we impose.

In this paper, we present the details of the modified code as well as a perturbative estimate of the efficiency of turbulent dissipation. In Section 2, we derive the anelastic approximation to the Navier–Stokes equations, modified to include a time-dependent shear, in Section 3 we present the numerical algorithm, in Section 4 we show the tests we ran to confirm that our implementation actually evolves the desired equations and verify that the numerical scheme is indeed second-order accurate in time, and finally, in Section 5 we use the perturbative calculation to get an estimate of the effective turbulent viscosity

in our simulated box and compare it with the results of Penev et al. (2009b).

## 2. THE EVOLUTION EQUATIONS

The fully compressible set of equations we would like to evolve, in a box-like domain, with the  $x$ - and  $y$ -axes perpendicular to the acceleration of gravity and the  $z$ -axis pointing against the gravity, are

$$\frac{\partial \mathbf{v}}{\partial t} = -\mathbf{v} \cdot \nabla \mathbf{v} - \frac{1}{\rho} \nabla p - g \hat{\mathbf{z}} + \mathbf{f}, \quad (3)$$

$$\frac{\partial \rho}{\partial t} = -\nabla \cdot \rho \mathbf{v}, \quad (4)$$

$$\frac{\partial \theta}{\partial t} = -\mathbf{v} \cdot \nabla \theta + \frac{\theta}{C_p T \rho} \nabla \cdot (\kappa \nabla T), \quad (5)$$

$$\theta = T \left( \frac{p_0}{p} \right)^{\frac{R}{C_p}}, \quad (6)$$

$$p = \rho R T, \quad (7)$$

where  $p$  is the pressure,  $T$  is the temperature,  $\rho$  is the density,  $\mathbf{v}$  is the velocity,  $\theta$  is the potential temperature,  $C_p$  is the specific heat at constant pressure,  $R$  is the ideal gas constant,  $g$  is the acceleration due to gravity,  $\kappa$  is the heat diffusion coefficient, and  $\mathbf{f}$  is some external forcing (e.g., tidal force).

As was said before, we do not actually evolve Equations (3)–(7), but rather their anelastic approximation. To develop the anelastic equations, each flow variable is split into a sum of a time-independent background component (denoted by an over bar) and a time-varying perturbation (denoted by tilde over its symbol) superimposed on top of that.

The background variables satisfy the above equations with all  $x$ ,  $y$ , and  $t$  derivatives set to zero and no velocity. The boundary conditions that complete these equations are that we require the background temperature on the top and bottom walls to have some fixed values  $T_{\text{low}}$  and  $T_{\text{high}}$ , respectively, and the pressure at the top wall to have some value,  $p_{\text{top}}$ .

Alternatively, we could fix the temperature gradients at the boundary, which would set the flux that the simulated convective layer must transport. Neither of those two options is exactly what the actual physical problem requires. We could base our boundary conditions on reliable physics, if we were planning to simulate the entire convective zone, however, this is impossible to do at the resolution required to study the turbulent dissipation, so we will ultimately be interested only in the flow that develops in the interior of the box and plan to exclude the regions near the top and bottom boundaries from any analysis we do. For this reason the choice of the exact thermal boundary conditions will hopefully have little impact on our results.

For convenience, we define the following quantities:

$$\mathcal{K}(z) \equiv \int_{-L_z/2}^z \frac{dz}{\kappa(z)} \quad (8)$$

$$\text{and } \alpha \equiv \frac{T_h - T_l}{\mathcal{K}(L_z/2)}, \quad (9)$$

where the  $z$  coordinate has a value  $-L_z/2$  at the bottom of the box and  $L_z/2$  at the top of the box.

The background variables that emerge as the solution to Equations (3)–(7) are

$$\bar{T} = T_h - \alpha \mathcal{K}, \quad (10)$$

$$\bar{\rho} = \frac{P_{\text{top}}}{RT_l} \exp \left[ \int_z^{L_z/2} \frac{1}{\bar{T}} \left( \frac{g}{R} - \frac{\alpha}{\kappa} \right) dz \right], \quad (11)$$

$$\bar{p} = \bar{\rho} R \bar{T}, \quad (12)$$

$$\bar{\theta} = \bar{T} \left( \frac{P_0}{\bar{p}} \right)^{\frac{R}{C_p}}. \quad (13)$$

To get the anelastic equations, we write all the variables in the original equations as a background and perturbation component:

$$p = \bar{p} + \tilde{p}, \quad (14)$$

$$\rho = \bar{\rho} + \tilde{\rho}, \quad (15)$$

$$T = \bar{T} + \tilde{T}, \quad (16)$$

$$\theta = \bar{\theta} + \tilde{\theta}. \quad (17)$$

Inserting Equations (14)–(17) in the fully compressible Equations (3)–(7) and dropping terms quadratic in the perturbation variables, we get the set of anelastic equations we would like to evolve with time:

$$\nabla \cdot \bar{\rho} \mathbf{v} = 0, \quad (18)$$

$$\frac{\partial \mathbf{v}}{\partial t} = \mathbf{v} \times \boldsymbol{\omega} - \nabla \tilde{h} + \frac{\tilde{\theta}}{\bar{\theta}} g \hat{\mathbf{z}} + \mathbf{f}, \quad (19)$$

$$\frac{\partial \tilde{\theta}}{\partial t} = -v_z \frac{d\tilde{\theta}}{dz} - \mathbf{v} \cdot \nabla \tilde{\theta} + \frac{\tilde{\theta}}{C_p \bar{T} \bar{\rho}} \nabla \cdot (\kappa \nabla \tilde{T}), \quad (20)$$

$$\tilde{h} \equiv \frac{\tilde{p}}{\bar{\rho}} + \frac{\mathbf{v}^2}{2}, \quad (21)$$

$$\frac{\tilde{p}}{\bar{p}} = \frac{\tilde{\rho}}{\bar{\rho}} + \frac{\tilde{T}}{\bar{T}}, \quad (22)$$

$$\frac{\tilde{\theta}}{\bar{\theta}} = \frac{\tilde{p}}{\bar{\rho} g H_\rho} - \frac{\tilde{\rho}}{\bar{\rho}}, \quad (23)$$

where we have introduced the enthalpy  $\tilde{h}$  (defined by Equation (21)), the density scale height  $H_\rho \equiv -\left(\frac{d \ln \bar{\rho}}{dz}\right)^{-1}$ , and the vorticity  $\boldsymbol{\omega} \equiv \nabla \times \mathbf{v}$ . Equation (23) is not the correct linearized equation for the potential temperature. The denominator of the pressure term should have been  $\gamma \bar{p}$  instead of  $\bar{\rho} g H_\rho$ . This replacement was introduced by Bannon (1996). He showed that it is required to ensure that the anelastic equations conserve energy.

Note that in Equation (20) we do not include a heat diffusion term proportional to the potential temperature gradient as is sometimes done in simulations of the solar convection to allow for some subgrid turbulent heat transport (cf. Clune et al. 1999).

To define the time evolution completely, we need to add boundary conditions to the above equations. The boundary conditions on the four vertical walls of the domain are set by the fact that we use Fourier series expansion for the horizontal dependence of all quantities, and hence we must impose periodicity in those directions. In addition to that, we want the temperature at the top and bottom boundaries to have the values we specified for  $\bar{T}$  ( $T_l$  and  $T_h$ , respectively), and hence

its perturbation should be zero. Also we require that the top and bottom walls are impermeable, but with no friction. That means that we set  $v_z$  to zero at the top and bottom boundaries and do not require anything for  $v_x$  and  $v_y$ .

The anelastic equations above obey a set of energy conservation equations for the following definitions of the kinetic and thermal energies:

$$E_K \equiv \int_V \bar{\rho} \frac{\mathbf{v}^2}{2} dV, \quad (24)$$

$$E_T \equiv \int_V C_p \bar{\rho} \bar{T} \frac{\tilde{\theta}}{\bar{\theta}} dV. \quad (25)$$

Using the anelastic evolution equations, the rates of change of these two energies can be shown to be

$$\frac{dE_K}{dt} = \mathcal{E}_1, \quad (26)$$

$$\frac{dE_T}{dt} = -\mathcal{E}_1 + \mathcal{E}_2, \quad (27)$$

where the sinks/sources are defined as

$$\mathcal{E}_1 \equiv g \int_V \frac{\bar{\rho}}{\bar{\theta}} \tilde{v} \tilde{\theta} dV, \quad (28)$$

$$\mathcal{E}_2 \equiv \int \left( \kappa \frac{\partial \tilde{T}}{\partial z} \Big|_{\frac{L_z}{2}} - \kappa \frac{\partial \tilde{T}}{\partial z} \Big|_{-\frac{L_z}{2}} \right) dx dy. \quad (29)$$

### 3. NUMERICAL TIME EVOLUTION

#### 3.1. Spectral Method

The spectral method used in this code is exactly the same as in Barranco & Marcus (2006, Section 3.2). For completeness we reproduce it below adopting their notation.

The spectral representation for a flow variable ( $q$ ) used in the code, at a resolution of  $N_x \times N_y \times N_z$  in the  $x$ -,  $y$ -, and  $z$ -directions, respectively, is given by

$$q(x, y, z, t) \approx \sum_{k=-\frac{N_x}{2}+1}^{\frac{N_x}{2}} \sum_{l=-\frac{N_y}{2}+1}^{\frac{N_y}{2}} \sum_{m=0}^{N_z} \hat{q}_{klm} \times (t) e^{i2\pi kx/L_x} e^{i2\pi ly/L_y} T_m(z), \quad (30)$$

where the vertical basis functions,  $T_m(z) \equiv \cos(m \cos^{-1} \frac{z}{L_z})$ , are Chebyshev polynomials. The numerical method we use does almost all calculations in the wavenumber/Chebyshev space, except for taking products of variables, which are done by first transforming back to physical ( $x, y, z$ ) space on a grid of collocation points, taking the product there and transforming back.

The grid of collocation points is defined by  $\{x_l = -L_x/2 + l\Delta x, y_m = -L_y/2 + m\Delta y, z_n\}$ , where  $\Delta x = L_x/N_x$  and  $\Delta y = L_y/N_y$ , and the vertical collocation points are defined by

$$z = \frac{L_z}{2} \cos(\xi), \quad \xi_n \equiv \frac{n\pi}{N_z}. \quad (31)$$

With this definition, the vertical Chebyshev basis functions of  $z$  are mapped to cosine basis functions in  $\xi$ :

$$T_m\left(\frac{2z}{L_z}\right) = \cos\left[m \cos^{-1}\left(\frac{2z}{L_z}\right)\right] = \cos(m\xi), \quad (32)$$

so with this choice of unevenly spaced  $z$  collocation points, the Chebyshev transform in the vertical direction can be computed as a discrete cosine transform in the evenly spaced  $\xi$  coordinate.

### 3.2. Time Integration

Time integration is performed using a fractional time step method. Each fractional step consists of updating the flow variables according to only one or several terms of the corresponding evolution equation, introducing as many steps as are necessary to incorporate all terms. Special care must be taken to ensure that the order of the fractional steps does not introduce spurious second-order terms that would render the time integration first-order accurate in time. Below we present the steps in the order in which they are performed in the code. In what follows, we will use superscripts to refer to the index of the time step, with fractional values corresponding to fractional steps.

#### 3.2.1. Advection Step

The advection step is fully explicit. It uses values from the current and previous time steps to achieve second-order accuracy. It first calculates the quantities

$$\mathfrak{M} \equiv \mathbf{v} \times \boldsymbol{\omega} + \frac{\tilde{\theta}}{\bar{\theta}} g \hat{\mathbf{z}} \quad (33)$$

$$\text{and } \mathfrak{N} \equiv -v_z \frac{d\tilde{\theta}}{dz} - \mathbf{v} \cdot \nabla \tilde{\theta}. \quad (34)$$

Then, the velocity and the temperature are updated according to

$$\mathbf{v}^{N+\frac{1}{3}} = \mathbf{v}^N + \frac{\Delta t}{2}(3\mathfrak{M}^N - \mathfrak{M}^{N-1}) \quad (35)$$

$$\text{and } \tilde{\theta}^{N+\frac{1}{3}} = \tilde{\theta}^N + \frac{\Delta t}{2}(3\mathfrak{N}^N - \mathfrak{N}^{N-1}). \quad (36)$$

#### 3.2.2. Hyperviscosity Step

The purpose of this step is to suppress the highest modes both in the horizontal and vertical directions, in order to avoid the buildup of power there due to the truncation of the spectrum at some finite number of spectral coefficients. For finite difference codes, a step of this sort is unnecessary, because there is some finite ‘‘grid viscosity,’’ associated with the numerical scheme, while for spectral codes, there is no equivalent effect. We implement the hyperviscosity step exactly in the way described in Barranco & Marcus (2006), suppressing each spectral coefficient by a factor as follows:

$$\mathbf{v}_{klm}^{N+\frac{2}{3}} = \mathbf{v}_{klm}^{N+\frac{1}{3}} \exp\left[-\Delta t \left(v_{\perp}^{\text{hyp}} k_{\perp}^{2p} + v_z^{\text{hyp}} m^{2p}\right)\right], \quad (37)$$

$$\theta_{klm}^{N+\frac{2}{3}} = \theta_{klm}^{N+\frac{1}{3}} \exp\left[-\Delta t \left(v_{\perp}^{\text{hyp}} k_{\perp}^{2p} + v_z^{\text{hyp}} m^{2p}\right)\right], \quad (38)$$

where  $v_{\perp}^{\text{hyp}}$  and  $v_z^{\text{hyp}}$  are some hyperviscosity coefficients,  $p$  is an integer between 1 and 6,  $k_{\perp}^2 \equiv k_x^2 + k_y^2$  is the horizontal wavenumber, and  $m$  is the order of the Chebyshev polynomial that this particular amplitude applies to.

Equation (37) is equivalent to adding a term to the right-hand side of the momentum Equation (3) of the form

$$\left(\frac{\partial \mathbf{v}}{\partial t}\right)_{\text{hyp}} = -\left\{v_{\perp}^{\text{hyp}} \left[\frac{\partial^2}{\partial x^2} + \frac{\partial^2}{\partial y^2}\right]^p + v_z^{\text{hyp}} \left[\sqrt{1-z^2} \frac{\partial}{\partial z} \left(\sqrt{1-z^2} \frac{\partial}{\partial z}\right)\right]^p\right\} \mathbf{v}. \quad (39)$$

The complicated  $z$  operator has been chosen to have the Chebyshev polynomials as its eigenfunctions. This replacement was suggested by Boyd (1998), because having an actual diffusion operator would raise the order of the differential equations and require the introduction of additional nonphysical boundary conditions at the top and bottom of the box.

In addition, choosing a large value for  $p$  (typically  $p = 6$ ) means that only the high spatial frequency modes will be affected, leaving the large-scale flow closer to inviscid, while still maintaining numerical stability.

This approach is different from what is often done in simulations of the solar convection where actual viscosity is introduced (cf. Chan & Sofia 1989; Cattaneo et al. 1991; Stein et al. 1989). This is sometimes necessary, especially if magnetic fields are considered, in order to have appropriate ratios between magnetic and molecular viscosity, for example.

Similarly, Equation (38) is equivalent to adding a term to the right-hand side of the temperature Equation (5) of the form

$$\left(\frac{\partial \tilde{\theta}}{\partial t}\right)_{\text{hyp}} = -\left\{v_{\perp}^{\text{hyp}} \left[\frac{\partial^2}{\partial x^2} + \frac{\partial^2}{\partial y^2}\right]^p + v_z^{\text{hyp}} \left[\sqrt{1-z^2} \frac{\partial}{\partial z} \left(\sqrt{1-z^2} \frac{\partial}{\partial z}\right)\right]^p\right\} \tilde{\theta}. \quad (40)$$

It is important to note that the introduction of this artificial hyperviscosity term breaks the conservation of energy in our box, since we do not add a corresponding heat source to replenish the energy lost.

#### 3.2.3. Pressure Step

The pressure step ensures that the velocity at the end of the time step satisfies the anelastic constraint—Equation (18). In the numerical scheme, we abandon the enthalpy at a specific time as a variable, and instead use its average between two consecutive time steps:

$$\Pi^{N+1} \equiv \frac{1}{2}(\tilde{h}^{N+1} + \tilde{h}^N). \quad (41)$$

We then achieve second-order accurate time evolution by updating the velocity according to

$$\mathbf{v}^{N+1} = \mathbf{v}^{N+\frac{2}{3}} - \frac{\Delta t}{2}(\nabla \tilde{h}^{N+1} + \nabla \tilde{h}^N) = \mathbf{v}^{N+\frac{2}{3}} - \Delta t \nabla \Pi^{N+1}. \quad (42)$$

Imposing the anelastic constraint, we get

$$\begin{aligned} 0 &= \nabla \cdot \mathbf{v}^{N+1} + v_z^{N+1} \frac{d \ln \bar{\rho}}{dz}, \\ &= \nabla \cdot \mathbf{v}^{N+\frac{2}{3}} - \Delta t \nabla^2 \Pi^{N+1} + v_z^{N+\frac{2}{3}} \frac{d \ln \bar{\rho}}{dz} - \Delta t \frac{\partial \Pi^{N+1}}{\partial z} \frac{d \ln \bar{\rho}}{dz}. \end{aligned} \quad (43)$$

Regrouping and requiring  $v_z|_{\pm L_z/2} = 0$ , we get the differential equation for updating  $\Pi$  with its boundary conditions:

$$\left[ \nabla^2 + \frac{d \ln \bar{\rho}}{dz} \frac{\partial}{\partial z} \right] \Pi^{N+1} = \frac{1}{\Delta t} \left( \nabla \cdot \mathbf{v}^{N+\frac{2}{3}} + v_z^{N+\frac{2}{3}} \frac{d \ln \bar{\rho}}{dz} \right) \quad (44)$$

$$\frac{\partial \Pi^{N+1}}{\partial z} \Big|_{\pm L_z/2} = \frac{1}{\Delta t} v_z^{N+\frac{2}{3}} \Big|_{\pm L_z/2}. \quad (45)$$

Equation (45) is imposed at the expense of the two highest Chebyshev modes of the momentum Equation (19). For details of the implementation of this step in our code, see Appendix A.

### 3.2.4. Heat Diffusion Step

The heat diffusion step updates the potential temperature according to

$$\tilde{\theta}^{N+1} = \tilde{\theta}^{N+\frac{2}{3}} + \frac{\Delta t}{2} \frac{\bar{\theta} R \kappa}{C_p \bar{p}} \left[ \nabla^2 + \frac{d \ln \kappa}{dz} \frac{\partial}{\partial z} \right] (\tilde{T}^N + \tilde{T}^{N+1}). \quad (46)$$

When we express  $\tilde{T}$  in terms of  $\mathbf{v}$ ,  $\tilde{h}$ , and  $\tilde{\theta}$ , this gives a second-order differential equation for  $\tilde{\theta}^{N+1}$ . In terms of the following definitions,

$$\mathfrak{P} \equiv -\frac{\alpha \bar{\theta}}{g \kappa \bar{T}} \left[ \nabla^2 - \frac{d \ln \kappa}{dz} \frac{\partial}{\partial z} + \frac{\kappa'^2}{\kappa^2} - \frac{\kappa''}{\kappa} \right] \left( \tilde{h} - \frac{v^2}{2} \right), \quad (47)$$

$$C_1 \equiv \frac{d \ln \kappa}{dz} - \frac{2g}{C_p \bar{T}}, \quad (48)$$

$$C_2 \equiv \frac{g}{C_p \bar{T}} \left( \frac{d \ln \bar{\theta}}{dz} - \frac{d \ln \kappa}{dz} \right), \quad (49)$$

$$C_3 \equiv -\frac{2C_p \bar{\rho}}{\kappa \Delta t}, \quad (50)$$

$$C_4 \equiv \frac{\alpha \bar{\theta}}{g \kappa \bar{T}}, \quad (51)$$

the equation we solve during this step is

$$\begin{aligned} & \left( \nabla^2 + C_1 \frac{\partial}{\partial z} + C_2 + C_3 \right) \tilde{\theta}^{N+1} =, \\ & = (\mathfrak{P}^{N+1} + \mathfrak{P}^N) - \left( \nabla^2 + C_1 \frac{\partial}{\partial z} + C_2 \right) \tilde{\theta}^N + C_3 \tilde{\theta}^{N+\frac{2}{3}}. \end{aligned} \quad (52)$$

This is a second-order equation for  $\tilde{\theta}^{N+1}$ , so we need two boundary conditions to make the solution unique. These come from the requirement that the temperature perturbation on the boundary vanishes  $\tilde{T}|_{\pm L_z/2} = 0$ . This requires

$$\tilde{\theta}^{N+1} \Big|_{\pm L_z/2} = C_4 \left( \tilde{h}^{N+1} - \frac{\mathbf{v}^2}{2} \right). \quad (53)$$

We see that the differential Equation (52) uses only the value of  $\Pi^{N+1}$ , but the boundary conditions need the value of the enthalpy at the updated time. There are two options of how to obtain this value. One is to keep track of the enthalpy from the

very beginning, and after each pressure step, update it according to

$$\tilde{h}^{N+1} = 2\Pi^{N+1} - \tilde{h}^N. \quad (54)$$

However, if the initial value of  $\tilde{h}$  is not perfectly set this prescription will lead to oscillations in the value of the enthalpy at the top and bottom boundaries. To illustrate this, assume that initially we set  $\tilde{h}^0$  to a value that is slightly higher than what it should be. Since  $\Pi^1$  is calculated without reference to the initial conditions, it will have the correct value. This will lead to  $\tilde{h}^1$  being slightly smaller, and so on. These oscillations are then translated to the interior of the box, through their effect on the potential temperature variable. Further, we found that the amplitude of these oscillations grows with time for all the cases we ran.

In order to avoid this problem, instead of introducing the additional variable  $\tilde{h}$ , with the only purpose of getting temperature boundary conditions, we use a second-order approximation to its value through  $\Pi$ :

$$\tilde{h}^{N+1} \approx \frac{1}{2} (3\Pi^{N+1} - \Pi^N). \quad (55)$$

The boundary conditions (Equation (53)) are then imposed by ignoring the differential Equation (52) at the top and bottom walls (where it does not make sense anyway). For the implementation details of this step, see Appendix B.

## 4. TESTS

Since all the Fourier transforms and differential operators are computed in exactly the same way as in Barranco & Marcus (2006), we refer to Section 4.1 of that paper for a discussion of the performance of the code. There are two main performance differences between our version of the code and Barranco & Marcus (2006). The first one is that the evaluation of the heat diffusion step requires the evaluation of four additional 3D fast Fourier transforms (FFTs), which are the slowest operation performed by their code. The second difference is the fact that we have allowed for a more general background density and heat diffusion profile. On one hand, this introduces several additional FFTs along the vertical direction, and more importantly solving an  $N_z \times N_z$  matrix  $N_x \times N_y$  times for every pressure, Greens, and heat diffusion time step, making these the slowest steps for us. However, none of these changes lead to a different scaling of the number of time steps calculated per unit time with the number of processors used, and the overall approximately linear scaling is preserved for computational grids with resolutions of at least  $128^3$  on up to 128 processors, which were the typical resolution and number of processors used.

Below, we present various tests we ran to confirm that the code is evolving the equations described above and that the numerical scheme employed is second-order accurate in time. We repeat all the tests that Barranco and Marcus performed to confirm our numerical scheme and add a test of the Brunt–Väisälä frequency in our box. Since this is the critical quantity that determines the transition from convective stability to instability, it is an essential test for the intended use of the code.

### 4.1. The Background State

Most of the tests we performed share the same background state, which is also the background we used for the final convective box simulation. The only time we modified it was

in order to simulate a convectively stable box and observe the buoyancy mode. Here we describe that background state.

We use a self-consistent non-dimensional set of units. Hence, the results apply for any choice of units.

The dimensions of the box are  $4 \times 4 \times 4$ , with a resolution of 128 collocation points per direction.

We need to choose the vertical profile of the heat diffusion coefficient. On the one hand, because the vertical grid spacing is very small near the boundaries, having large  $v_z$  in those regions would mean that the CFL stability condition would impose an extremely small time step. In order to avoid this, we need to set up a background that is convectively stable near those boundaries. On the other hand, we would like to simulate top-driven convection, which is typical for stars with surface convection zones. To achieve that we need the most unstable stratification to occur near the top of the box. Because most of the driving appears near the top of the box and the density is much higher near the bottom of the box, we found that it was sufficient to have a convectively stable stratification only near the top wall. Further, since the heat diffusion step uses the heat diffusion coefficient, and its first and second derivatives, we need our expression for the heat diffusion coefficient to have a continuous second derivative.

To achieve all these requirements, we construct the particular  $\kappa(z)$  profile used in this paper from six separate pieces as follows:

$$\kappa(z) = \begin{cases} \kappa_0, & z < z_0 \\ \kappa_1 + \kappa_2 \sin[k(z - z_0)], & z_0 < z < z_1 \\ \kappa_3 + \kappa_4(z - z_1) \left[ \left( \frac{z - z_1}{z_2 - z_1} \right)^2 - 3 \right], & z_1 < z < z_2 \\ \kappa_5 + \kappa_6(z - z_2)^2 + \kappa_7(z - z_2)^3 + \kappa_8(z - z_2)^4, & z_2 < z < z_3 \\ \kappa_9 + \kappa_{10} \sin \left( \pi \frac{z - z_3}{z_4 - z_3} \right) + \kappa_{11}(z - z_3), & z_3 < z < z_4 \\ \kappa_{12}, & z_4 < z \end{cases}, \quad (56)$$

where the parameters  $\kappa_i$ ,  $i = 1 \dots 12$ ,  $z_j$ ,  $j = 1 \dots 4$ , and  $k$  are chosen to make  $\kappa$ ,  $\kappa'$ , and  $\kappa''$  continuous and to select the shape of the curve. The shape of the curve used in this article was determined from the following constraints.

1. The values that  $\kappa(z)$  takes at the boundaries:  $\kappa_0 = 20$  and  $\kappa_{12} = 21$ .
2. The depth above which  $\kappa(z)$  remains at its maximum value of  $\kappa_{12}$ :  $z_4 = 1.95$ .
3. The depth at which  $\kappa(z)$  has a minimum and the value at that minimum:  $z_2 = 1.4$  and  $\kappa(z_2) = 19.8$ .
4. The depth below which  $\kappa(z)$  is held constant at its bottom value of  $\kappa_0$ :  $z_0 = -1.8$ .
5. The locations of the two inflection points:  $z_1 = 0.2$  and  $z_3 = 1.85$ .

A plot of the resulting depth dependence of  $\kappa(z)$  is presented in Figure 1(a).

Next, we need to choose values for the background temperature at the top ( $T_{\text{low}}$ ) and bottom ( $T_{\text{high}}$ ) of the box. Those are dictated by the requirement that the flow speeds should never approach the local speed of sound; otherwise, the anelastic approximation is no longer acceptable, and the fully compressible equations should be used.

Finally, we need to choose values for the pressure at the top of the box ( $p_{\text{top}}$ ), the external gravity ( $g$ ), the specific heat at constant pressure ( $C_p$ ), and the value of the ideal gas constant ( $R$ ). These values together with  $T_{\text{low}}$  determine the pressure

and density scale heights. Since we are interested in studying turbulence in a stratified medium we need to choose these values such that our box encompasses at least several pressure and density scale heights. The particular values we use are

$$p_{\text{top}} = 1.0 \times 10^5, \quad (57)$$

$$g = 2.74, \quad (58)$$

$$C_p = 0.21, \quad (59)$$

$$R = 8.317 \times 10^{-2}, \quad (60)$$

$$T_{\text{low}} = 10.0, \quad (61)$$

$$T_{\text{high}} = 62.37. \quad (62)$$

We deliberately do not include any units in the above quantities, since the simulated flow is independent of the choice of units.

The resulting background potential temperature, pressure, and density are presented in Figures 1(b)–(d). One can see that the steepest negative slope of  $\bar{\theta}$  occurs for heights between 1 and 1.5 units and that significant stratification is imposed. From Figures 1(c) and (d), we see that the convective box encompasses 2.8 density scale heights and 4.6 pressure scale heights.

## 4.2. Energy

We first verify that the energy-like conserved quantities defined in Equations (24) and (25) evolve according to Equations (26)–(29). The initial conditions we used for this test were that all components of the velocity were set to 0, and the initial potential temperature contained random fluctuations in the lower 10% of the spectral modes. We chose the time step to be much smaller than the smallest absolute value of the buoyancy period, which in this case is an imaginary quantity for most of the box. This way, the time step is short both compared to the growth rate of the instability near the middle of the box and the  $g$ -mode period near the boundaries.

The test was performed by running the code with no hyperviscosity, which does not conserve energy. The kinetic and thermal energies, as well as the rates  $\mathcal{E}_1$  and  $\mathcal{E}_2$ , were saved at every time step. We then compute the time integrals of  $\mathcal{E}_1$  and  $\mathcal{E}_2$  using Simpson's method. This is sufficient, since the numerical evolution is only second-order accurate in time. In Figure 2, we show that Equations (26)–(29) are indeed satisfied to one part in a million.

## 4.3. Normal Modes

A second test we performed was checking that the normal modes of the linearized equations of motion evolve as expected. We look for normal modes of the form

$$\tilde{q}(x, y, z, t) = \hat{q}(k_x, k_y, z) e^{-i\omega t + ik_x x + ik_y y}. \quad (63)$$

For convenience, define

$$\hat{t} \equiv g \frac{\hat{\theta}}{\bar{\theta}}, \quad (64)$$

$$\omega_B^2 \equiv g \frac{d \ln \bar{\theta}}{dz}. \quad (65)$$

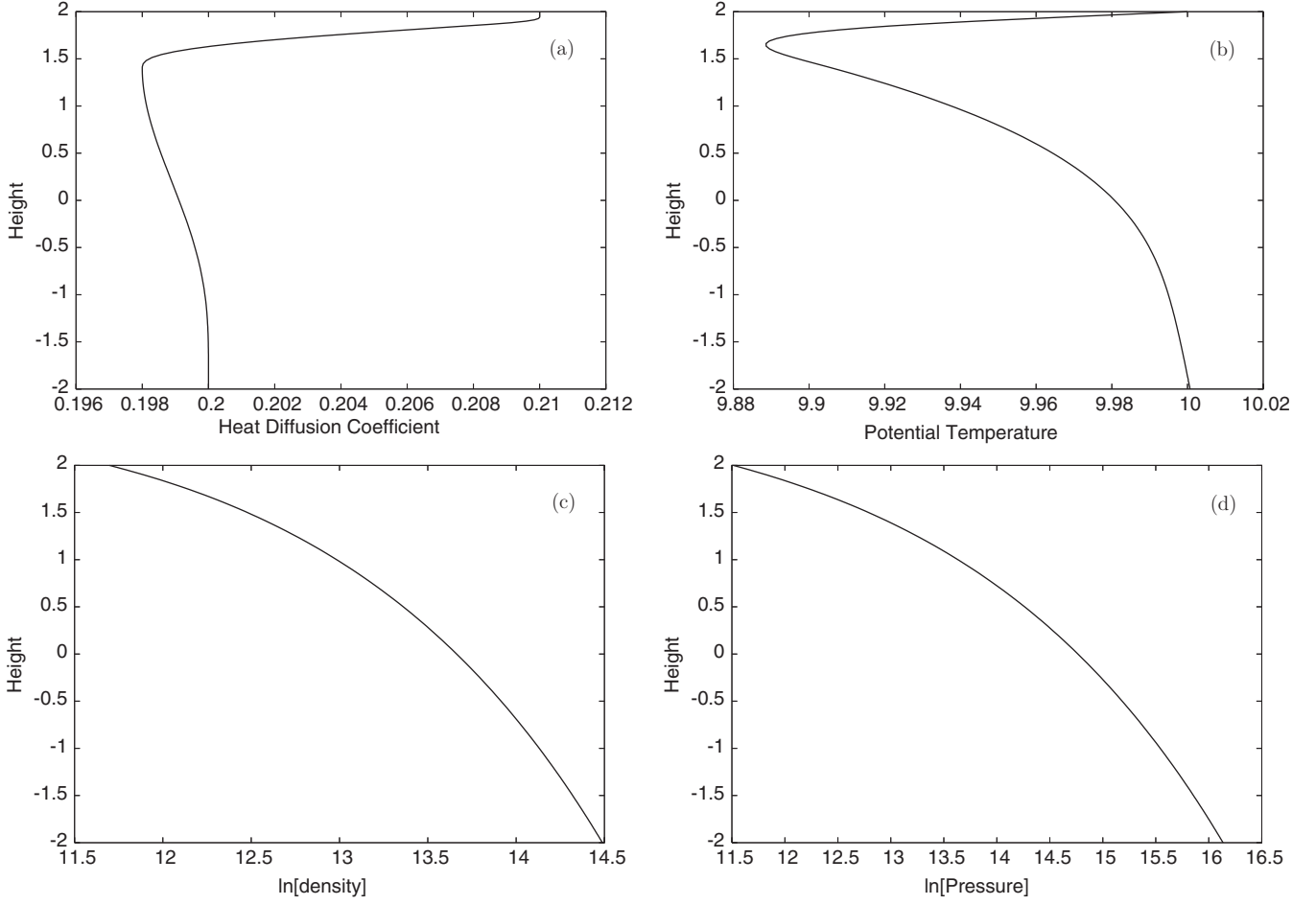


**Figure 1.** (a) Heat diffusion coefficient ( $\kappa$ ), (b) the background potential temperature ( $\bar{\theta}$ ), (c) the background density ( $\bar{\rho}$ ), and (d) the background pressure ( $\bar{p}$ ) profiles.

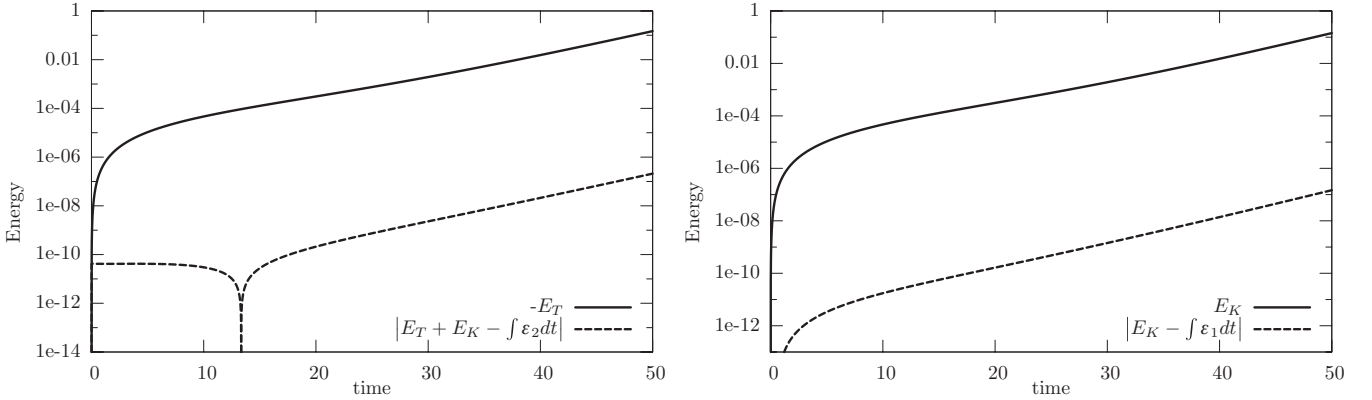


**Figure 2.** Energy conservation. Left: negative thermal energy—solid line, the absolute difference between the total energy calculated directly and as the integral of  $\mathcal{E}_2$ —dashed line. Right: kinetic energy (solid line), the absolute difference between the kinetic energy calculated directly and as the integral of  $\mathcal{E}_1$ —dashed line.

In terms of Equations (63)–(65), after dropping all nonlinear terms, the anelastic Equations (18)–(23) simplify to include only two variables  $\hat{v}_z$  and  $\hat{\tau}$ :

$$-i\omega \left( I - \frac{DD_A}{k_\perp^2} \right) \hat{v}_z = \hat{\tau} \quad (66)$$

$$-i\omega (\hat{\tau} + \mathcal{L}_1 \hat{v}_z) = -\omega_B^2 \hat{v}_z + \mathcal{L}_2 \hat{\tau}, \quad (67)$$

where the operators  $D$  and  $D_A$  are defined in Appendix A, Equations (A4) and (A5), and (with  $k_\perp^2 \equiv k_x^2 + k_y^2$ ) the operators

$\mathcal{L}_1$  and  $\mathcal{L}_2$  are

$$\mathcal{L}_1 = \frac{\alpha R}{C_p \bar{p}} \left[ \frac{1}{k_\perp^2} \left( \frac{\kappa'^2}{\kappa^2} - \frac{\kappa''}{\kappa} \right) D_A - \frac{d \ln \kappa}{dz} - \frac{d \ln \bar{\rho}}{dz} \right], \quad (68)$$

$$\mathcal{L}_2 = \frac{\kappa}{C_p \bar{\rho}} \left[ -k_\perp^2 - \frac{\alpha}{\kappa T} \frac{d \ln \kappa}{dz} + \left( \frac{d \ln \kappa}{dz} - \frac{\alpha}{\kappa T} \right) D + D^2 \right]. \quad (69)$$

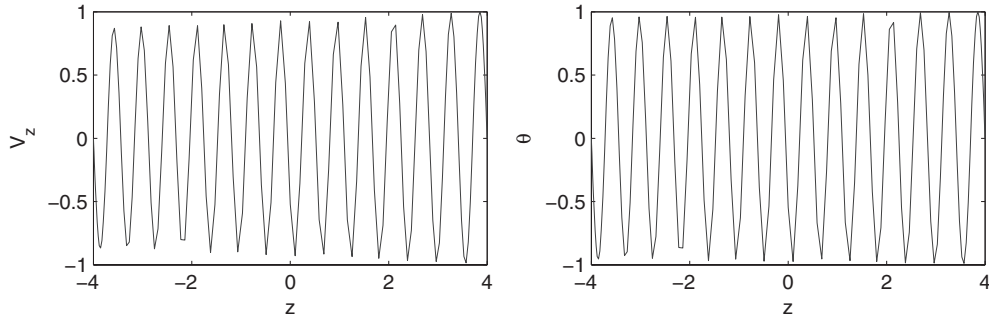


**Figure 3.** Example of the shape of the normal modes, we initialized the box with. On the left is the  $\hat{z}$  component of velocity and on the right is the potential temperature.

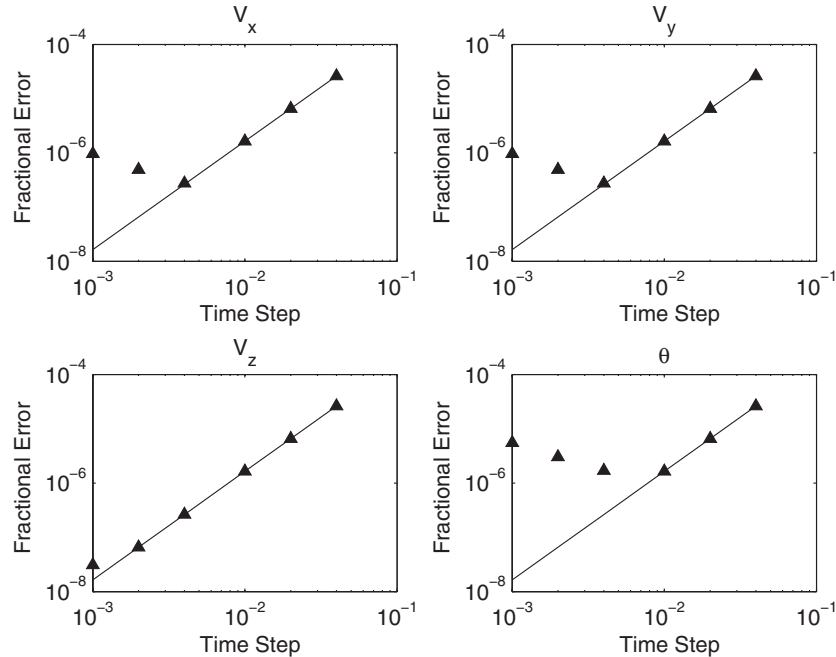


**Figure 4.** Maximum error in normal mode evolution, after a fixed evolution time. The error is scaled by the maximum value of the quantity at time  $t = 0$ . The solid line corresponds to quadratic scaling of the error with the time step.

In terms of  $\hat{v}_z$  and  $\hat{t}$  the remaining flow variables can be expressed as

$$k_{\perp}^2 \hat{h} = i\omega D_A \hat{v}_z, \quad (70)$$

$$i\omega \hat{v}_x = ik_x \hat{h}, \quad (71)$$

$$i\omega \hat{v}_y = ik_y \hat{h}. \quad (72)$$

We calculated several numerical solutions to the eigenmode equations (see Figure 3) and supplied them as initial conditions with very low amplitude to the code. We expect that for later times the evolution is done simply by multiplying the initial amplitudes by  $e^{-i\omega t}$ . We ran the code with the background discussed above, and a time step that was no larger than  $\frac{\pi}{250\omega}$  for the mode in question. The comparison with the simulated evolution of one of these eigenmodes is presented in Figure 4. As we can see, for large enough time steps, the error scales as the square of the time step, which confirms that the code is indeed second-order accurate in time at least as far as the linear terms are concerned. For very small time steps, the error deviates from that scaling due to numerical round off. The minimal fractional error is much larger than the numerical precision, because we

have chosen the heat diffusion to be as small as possible, which causes the matrix we invert during the heat diffusion step to have values along the diagonal that are many orders of magnitude larger than the off-diagonal values, which causes the numerical round off to be amplified many times. This also explains why the error in the potential temperature is the largest: the other variables suffer from this only indirectly.

#### 4.4. 2D Vortices

Another test we performed was initializing the box with a pair of circular columns of vorticity running from the top to the bottom boundary. In physical space, for each column the vorticity was constant and in the  $\pm \hat{z}$  direction. The two columns had opposite signs of vorticity, in order to ensure that the total vorticity in the box is zero, as required by the periodic boundary conditions (see the left panel of Figure 5). Evolving the system forward in time, one expects that the two vortices will remain stable, although distorted to a small extent, and move parallel to each other at a constant rate determined by the distance between them and the magnitude of their vorticity. In Figure 5, we show snapshots of a horizontal cross section of the vorticity in our box at different times. With  $t_{\text{cross}}$  denoting the expected box crossing time, the left panel shows the initial conditions, the middle

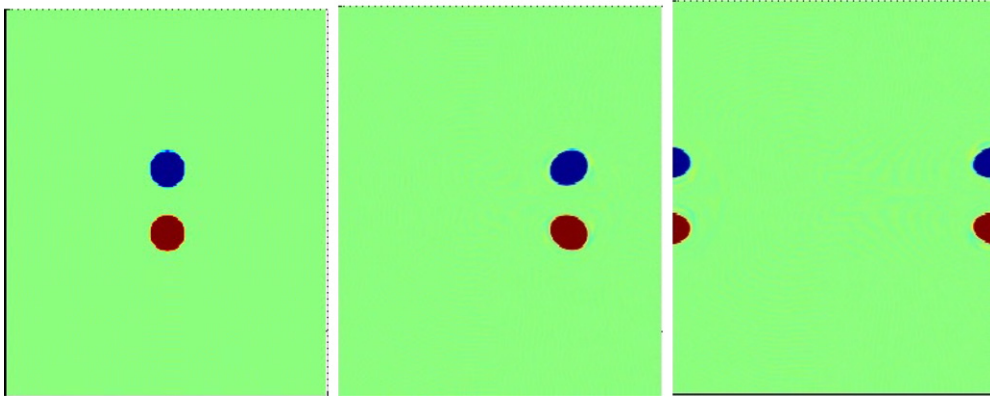


**Figure 5.** Snapshots at three different times of horizontal slices of the vorticity in the 2D vortices simulation. Red corresponds to positive vorticity, blue to negative, and green to zero. The left panel is at the start of the simulation, the middle at a little more than  $t_{\text{cross}}/4$ , and the right at  $t_{\text{cross}}/2$ .

(A color version of this figure is available in the online journal.)

panel corresponds to a little more than  $t_{\text{cross}}/4$ , and the right panel corresponds to  $t_{\text{cross}}/2$ . Because of the periodic boundary conditions, having two vortices in our box is equivalent to having an infinite number of vortices, copies of the two in the box. There is no analytical expression for the infinite series that determines the speed with which each column should move, but if the two vortices are far away from the walls as compared to the distance between them we expect that their motion is at least approximately that of the situation with only two vortices. The time step we chose in this case was  $0.005t_{\text{cross}}$ .

The difference between the actual and expected position of average absolute vorticity in the box is shown in Figure 6. We see that the average rate with which the vortices are moving is the correct rate. The oscillations evident in the figure are due to the deformation of the vortices from their initial cylindrical shapes. The drop at the end of the simulated time interval is due to the fact that, at this time, the vortices are leaving the box from the right boundary and their periodic copies are entering from the left (the last panel of Figure 5).

#### 4.4.1. Convectively Stable Box

The last test we performed was imposing a convectively stable stratification in the box and initializing with random temperature perturbations. In this case, one expects to see buoyancy oscillations with a frequency given by the Brunt–Väisälä frequency:  $\omega_B^2 \equiv g \frac{d}{dz} \ln \theta$ . So for this test, we needed the buoyancy frequency to be approximately constant throughout the box, and much larger than the time step, but small enough to allow us to simulate many buoyancy periods. So, we made the heat diffusion coefficient constant throughout the box and set the top and bottom temperatures to be the same. This way the buoyancy frequency is independent of height. The particular values for the parameters of this run were

$$p_{\text{top}} = 1.0 \times 10^5, \quad (73)$$

$$g = 2.0, \quad (74)$$

$$C_p = 0.2, \quad (75)$$

$$R = 8.317 \times 10^{-2}, \quad (76)$$

$$T_{\text{low}} = 10, \quad (77)$$

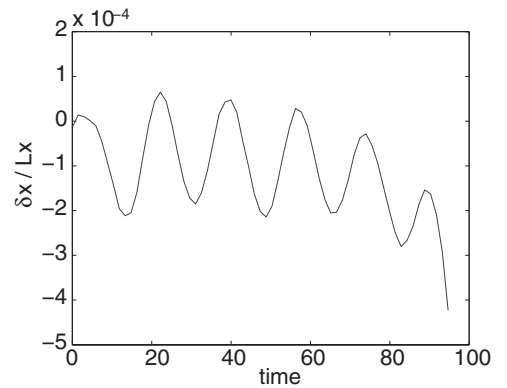


**Figure 6.** Difference between expected vortex position and the average position of vorticity. The period of the oscillations corresponds to the rotational period of the vortices and the drop in the end is due to the fact that the vortices are exiting the box on the right and hence a bit of them is appearing from the left, causing the average position of vorticity to move toward zero.

$$T_{\text{high}} = 10, \quad (78)$$

$$\delta t = 2 \times 10^{-3}, \quad (79)$$

giving a buoyancy frequency of  $\omega_B^2 = 2.0$ ,

A plot of the kinetic energy for this run is presented in Figure 7. It can be seen that, as expected, the kinetic energy goes through two cycles every buoyancy period. This is because the velocity has to go through one cycle, and the energy has a maximum every time the velocity has a maximum, or a minimum. The decay in the curve is caused mostly by the heat diffusion smoothing out the perturbations over time. Since different modes decay at different rates, and they are coupled through the nonlinear terms, we have not shown an expected decay curve.

## 5. ESTIMATING THE DISSIPATION IN AN UNSTABLY STRATIFIED CONVECTIVE BOX

### 5.1. Steady-state Flow

Having confirmed that the code is solving the correct equations, we simulated a box with the background state described in Section 4.1 for long enough to reach a steady state. In order to minimize the impact that the artificial hyperviscosity step has on our flow, we chose the smallest values of  $\nu_{\perp}^{\text{hyp}}$  and  $\nu_z^{\text{hyp}}$ ,

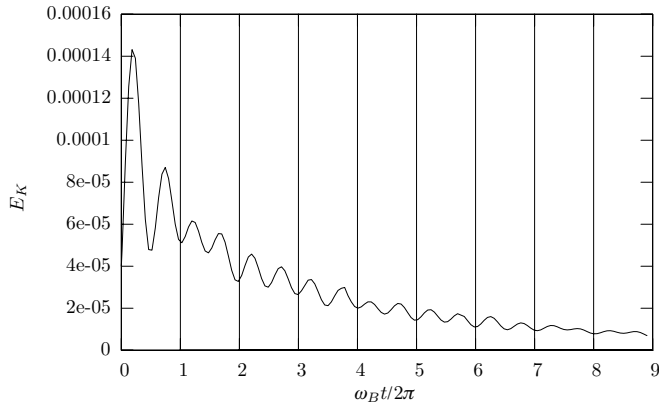


**Figure 7.** Kinetic energy as a function of time for a convectively stable box. The distance between every two consecutive vertical lines is the buoyancy period. The horizontal axis is time in units where the buoyancy period is 1.

separately for the temperature and the velocity that result in a numerically stable solution for the particular choice of resolution and temperature gradient, and we fix the hyperviscosity  $p$  parameter to 6, which means that only the highest few spectral coefficients are significantly affected by the hyperviscosity step. This is sufficient, since as we discussed earlier that numerical instability is due only to the two highest spectral modes growing exponentially. We also verified that the global properties of the flow—the equilibrium kinetic and thermal energies as well as the spatial power spectra of the velocity components and the potential temperature do not change if we double the  $\nu^{\text{hyp}}$  values.

We used two criteria for determining that a steady state has been reached. First, the kinetic and thermal energies should stop drifting systematically up or down, see Figure 8. The oscillations we see in the kinetic energy have a period close to the convective turnover time of the box. Second, the spatial spectra of the velocity and potential temperature must be steady to within a few percent.

The vertical spectra are not directly obtained from the output of the simulation since the collocation points of the computational grid are not evenly spaced, and the vertical direction is not periodic. We first re-sample to an evenly spaced grid and apply some window function, before performing the discrete Fourier transform. Since in the vertical direction we

simulate the Chebyshev series of the quantities, the most natural way to re-sample to an even grid is to evaluate this series for each of the new collocation points.

Fourier power spectra of the three velocity components and the potential temperature are presented in Figure 9, along with the scaling that Kolmogorov statistics predict (spectral power  $\propto k^{-5/3}$ ).

The sharp cutoff at high wavenumbers is due to the finite resolution of the box (using a box of half the resolution produces a cutoff at half the wavenumber we see in Figure 9). It is not directly due to the hyperviscosity, since reducing the value of  $\nu^{\text{hyp}}$  does not decrease its slope, but rather causes the highest few spectral components to grow exponentially with time, and only after they have grown to values higher than the spectrum before the cutoff, is power pumped to intermediate wave numbers, eliminating this cutoff.

Horizontal cross sections of  $v_z$  and  $\tilde{\theta} + \bar{\theta}$  at three different heights of a typical steady-state frame of the flow are presented in Figure 10. The three heights we chose were  $z = 1.98$ ,  $z = 0$ , and  $z = -1.98$  for a box in which the vertical coordinate runs from  $-2$  to  $2$ . Horizontal sections of the  $\hat{z}$  component of the vorticity  $\omega_z$  as well as typical vertical sections of the above quantities are presented in Figure 11.

Near the top boundary of the box (Figures 10(a) and (d)), the flow exhibits a cellular pattern of narrow down-flow lanes. Traces of the cells are visible only in the top 5% of the box, after that the flow organizes itself into a pair of perpendicular down-flow lanes that horizontally span the entire box. With time, those lanes get distorted, break up, and reform, but are well defined for at least half the time, for most of the upper half of the box. They are generally parallel to the grid  $x$ - and  $y$ -axes.

Similar patterns were first observed by Porter & Woodward (2000). Their tests show that the lanes tend to align themselves with the periodic directions of the models and not with the grid axis per se (rotating the periodic directions at  $45^\circ$  relative to the grid axis caused the lanes to rotate as well). So they conclude this to be due to the small horizontal to vertical aspect ratio of the simulations.

Around the middle of the box, the pair of perpendicular lanes are still sometimes visible, but they are a lot less persistent. Rather, at those depths, the flow consists of one or two down-flows, which take up less than a quarter of the cross-sectional area, the rest being occupied by a gentler up-flow (Figures 10(b) and (e)).

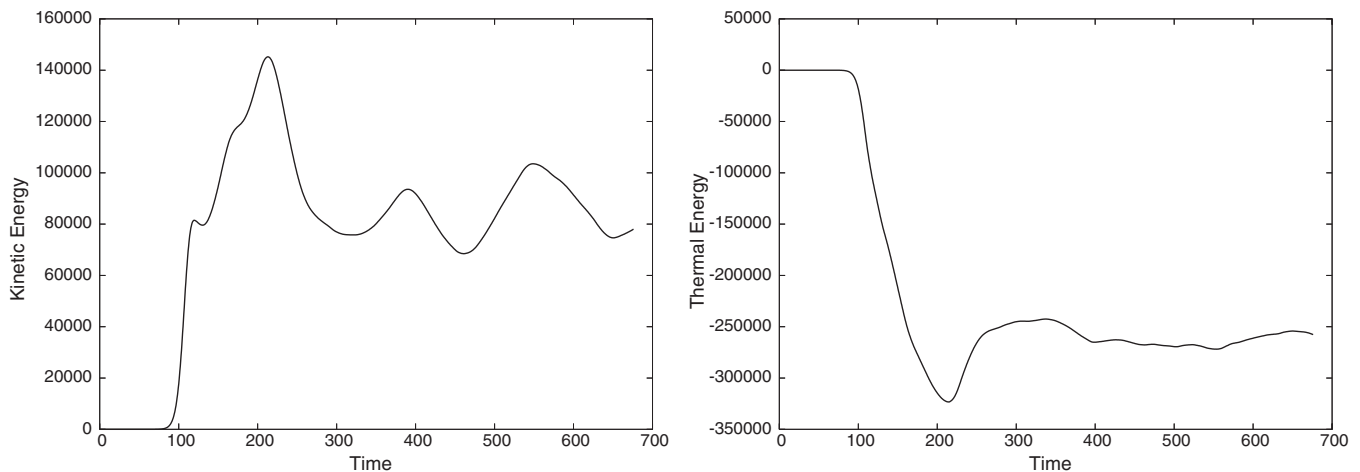


**Figure 8.** Kinetic (left) and thermal (right) energy content of the convective box used as one of the criteria for having reached a steady state. We decided that steady state was reached at a time of 400.

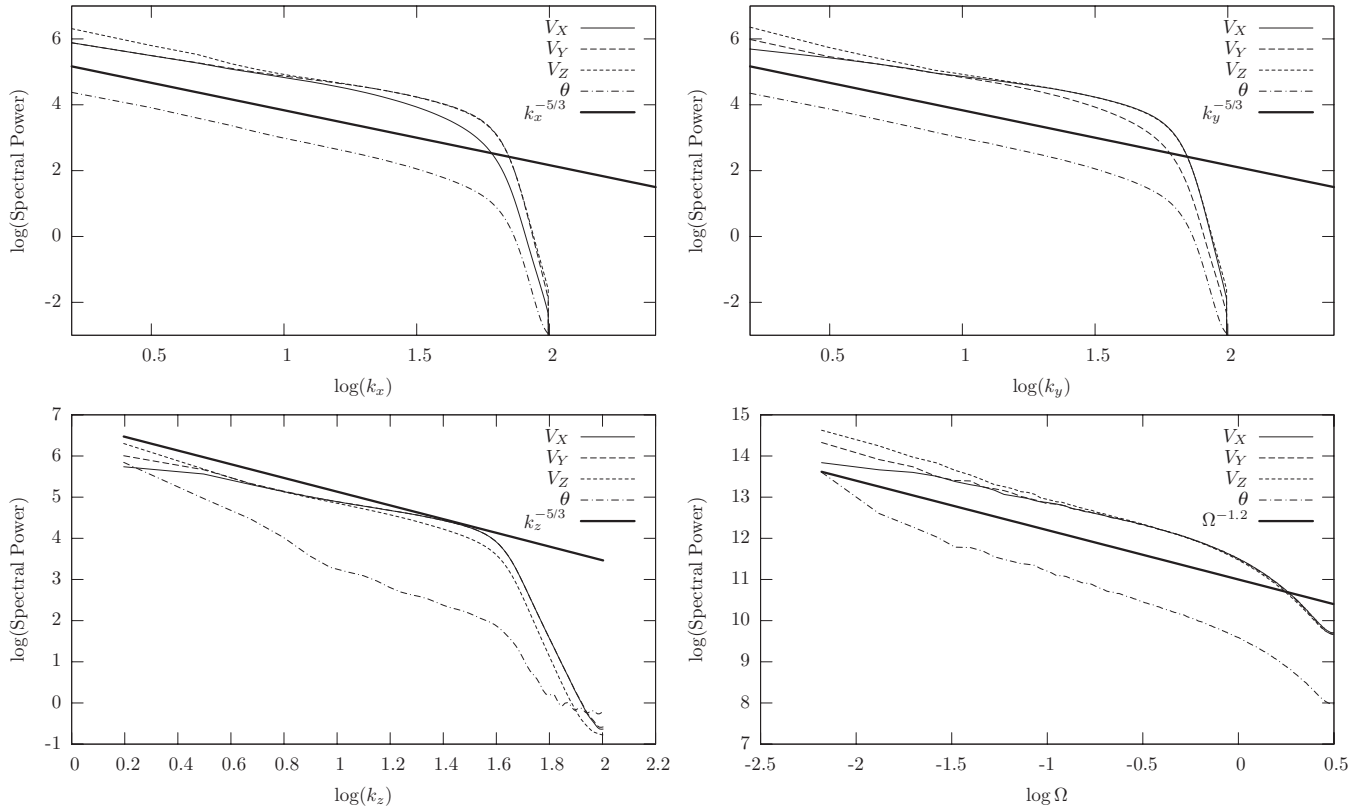


**Figure 9.** (x: top left; y: top right; z: bottom left; time: bottom right) Spectra of the three velocity components and the potential temperature. The thick line corresponds to Kolmogorov scaling ( $E_k \propto k^{-5/3}$ ) in the first three plots and to the scaling we find for the effective viscosity (see the next section) in the last plot.

For the lower half of the box, the asymmetry between up- and down-flows gradually decreases as we get further down. Near the bottom boundary the large scale of the flow disappears, until only small-scale structure is left (Figures 10(c) and (f)).

This behavior with depth of the convective structures seems to be a general more or less scale independent property of stratified convection. It is seen both in local simulations (e.g., Porter & Woodward 2000) and in global ones.

Since we ran our simulations with the smallest possible value of the heat diffusion coefficient, we expect to have efficient convection, hence we would expect the  $z$  gradient of the potential temperature to be very close to zero except near the impenetrable top and bottom boundaries. The averaged over time and horizontal directions logarithmic gradient of  $\tilde{\theta} + \bar{\theta}$  can be seen in Figure 12. As we can see, the scale height of  $\theta$  is indeed more than two orders of magnitude larger than the box, as long as we are not very close to the boundaries. The top of the box has a local minimum of the entropy gradient and a significant convectively stable region, so as to keep the large magnitude vertical flow from getting too close to the boundary and causing numerical problems. We also see that another local minimum of the entropy gradient has developed near the bottom of the box. This is caused by the lower impenetrable wall. Not having a significantly thick convectively stable region near the bottom is acceptable, because the larger density of the fluid means that the flow velocities are much smaller than at the top of the box, and thus the CFL condition near the bottom wall gives a lot less stringent limitation on the time step.

### 5.2. Adding Units

If one wants to compare our values to physical conditions, in, for example, the solar convective zone, one needs to select a

**Table 1**

Example Set of Units Applied to the Unstably Stratified Simulation

Quantity	Unit
Length	$10^8$ cm
Time	10 s
Mass	$10^{14}$ g
Temperature	1000 K

particular set of units in which all the variables will be expressed. Of course, the results are equally applicable to any choice, but here we present one, converting all quantities discussed above for the unstably stratified case just as an illustration. The particular choice we make is shown in Table 1.

This would make our simulated box have dimension of 4 Mm, densities ranging from  $10^{-5}$  to  $2 \times 10^{-4}$  g cm $^{-3}$ , and pressures in the range of  $10$ – $10^3$  bar. The gravity we impose then would be  $2.74 \times 10^4$  cm s $^{-2}$  (exactly the solar surface gravity), the typical convective velocities that develop in our convective zone are a few km s $^{-1}$ , the convective turnover time is on the order of 1000 s, and the flux transported by our box, estimated as the diffusive heat flux through the bottom boundary:  $\kappa(dT/dz)_{-L_z/2} = 2.8 \times 10^{11}$  erg s $^{-1}$  cm $^{-2}$  or about four times the solar surface flux. So in this set of units, the simulated flow looks similar to the actual flow a bit under the solar photosphere, at least in gross terms.

### 5.3. Lowest Order Perturbative Expansion

Ignoring the part of the simulation before steady state was reached, we applied the perturbative method of Goodman & Oh (1997) as described by Penev et al. (2009b) to find a lowest order perturbative expansion estimate of the energy transfer rate

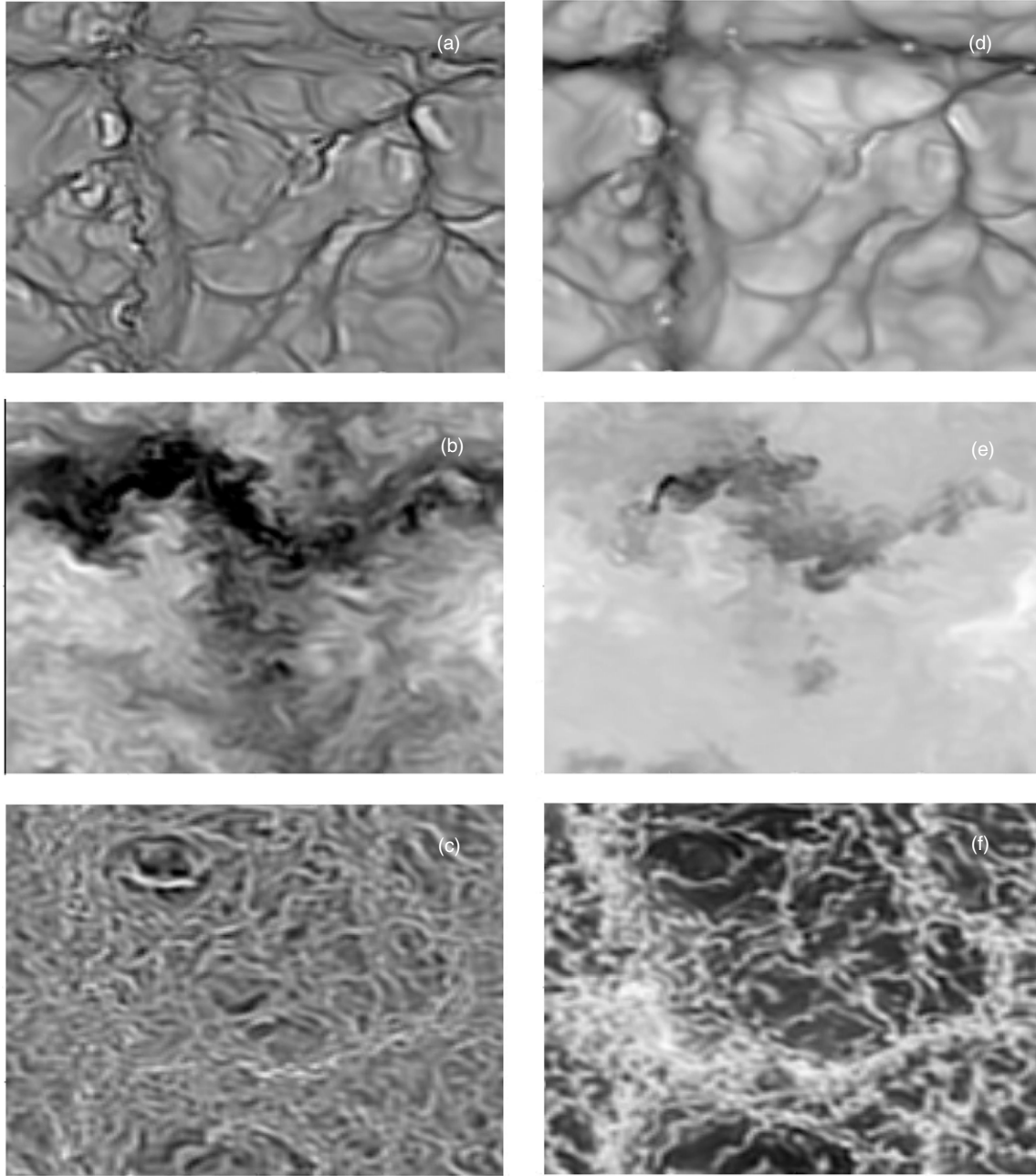


**Figure 10.** Horizontal cross sections of the vertical velocity component (left) and the total potential temperature (right) at three different heights of the box:  $z = 1.98$  (a, d),  $z = 0$  (b, e), and  $z = -1.98$  (c, f). Darker areas correspond to lower values, with the gray scale in each figure adjusted to the range of values encountered in the slice.

between a small amplitude external forcing and the turbulent flow in our box, and, respectively, from that we can derive the components of an effective viscosity tensor that reproduces the energy dissipation rate due to the turbulence.

We assume forcing in the form of an external velocity field:

$$\mathbf{V} = \mathbf{A}(t) \cdot \mathbf{x}. \quad (80)$$

Goodman & Oh (1997) define two dimensionless parameters: the tidal strain  $\Omega^{-1} |\mathbf{A}|$  and  $(\Omega \tau_c)^{-1}$ , where  $\Omega$  is the frequency of the perturbation and  $\tau_c \equiv L_c / V_c$ . The characteristic convective length scale is  $L_c$  and  $V_c$  is the characteristic convective velocity. In the case of hierarchical eddy structured convection  $\tau_c$  is the eddy turnover time.

We then take only the lowest nonzero term in the expansion of the energy transfer rate  $\mathcal{E}$  with respect to those two parameters. The resulting expression is

$$\begin{aligned} \dot{\mathcal{E}}(\Omega = 2\pi R/T) &= \text{Re}\{S_{R,-R} + S_{R,R}\} \\ &+ \sum_{r \neq 0} \frac{1}{\pi r} \text{Im}\{S_{r+R,r-R} + S_{r+R,r+R}\}, \quad (81) \end{aligned}$$

$$\text{with } S_{\rho,\rho'} \equiv \frac{T}{\mathcal{N}^2 N_z} \sum_{\lambda,\mu,\nu,\nu'} \rho_{\nu-\nu'}^* v_{\lambda,\mu,\nu,\rho}^1 P_{\lambda,\mu,\nu} v_{\lambda,\mu,\nu',\rho'}^{2*},$$

where  $\mathcal{N} \equiv N_x N_y N_z N_t$ ,  $P_{\lambda,\mu,\nu} \equiv \mathbf{I} - \mathbf{k}'_{\lambda,\mu,\nu} \mathbf{k}'_{\lambda,\mu,\nu} / k_{\lambda,\mu,\nu}^2$ , with  $\mathbf{k}'_{\lambda,\mu,\nu} \equiv k_{\lambda,\mu,\nu} + \hat{z}/H_\rho$ ,  $\rho(k_z)$  is the Fourier transform of the density averaged over  $x, y, t$ .

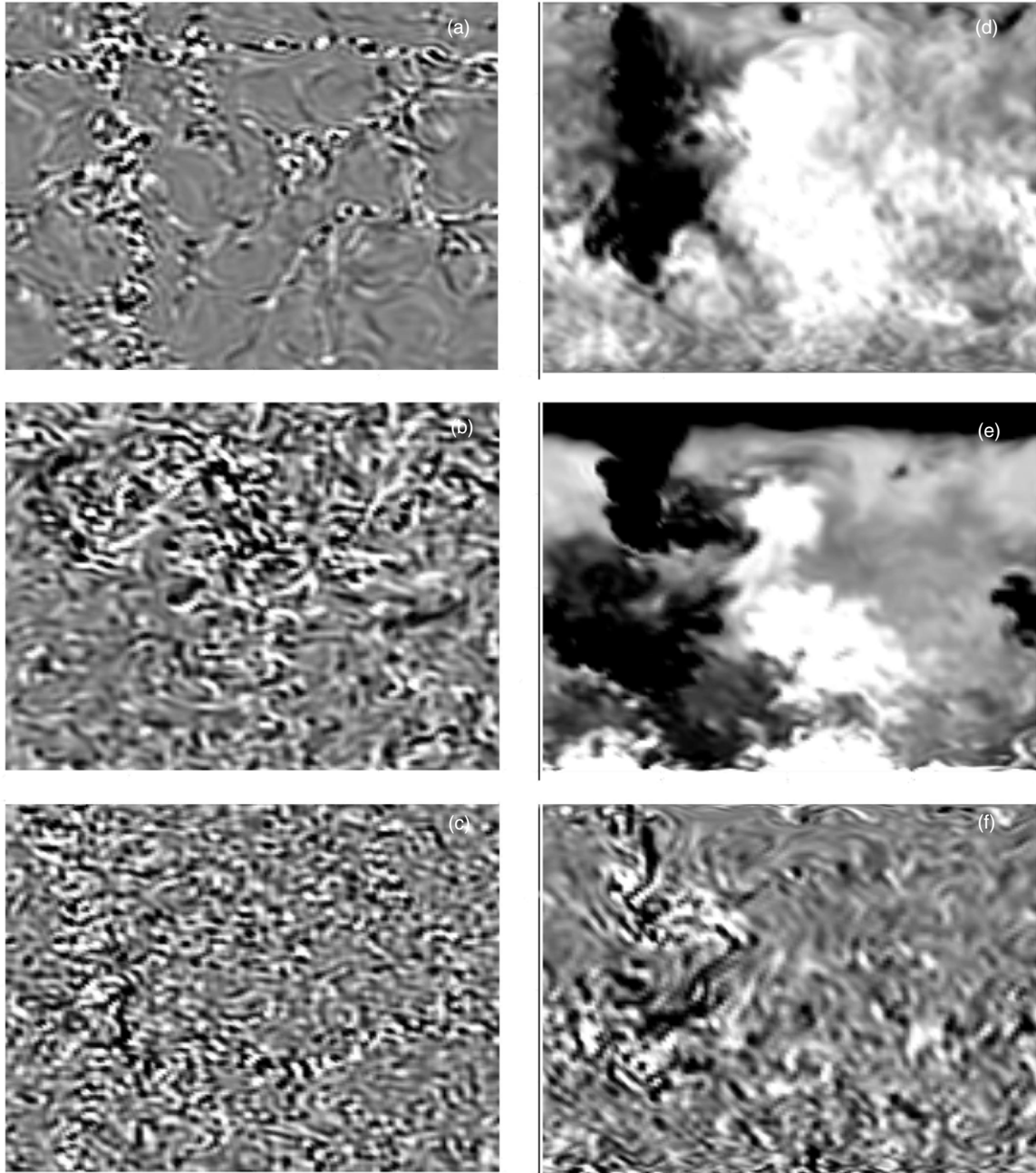


**Figure 11.** Horizontal cross sections of the vertical vorticity component (left panels) at heights:  $z = 1.98$  (a),  $z = 0$  (b), and  $z = -1.98$  (c). Vertical cross sections (right panels) of the vertical velocity (d), the total potential temperature (e), and the vertical vorticity (f). Darker areas correspond to lower values, with the gray scale in each figure adjusted to the range of values encountered in the slice.

In this case, we do not need to worry about the compressibility of the flow, since the anelastic approximation does not allow for any. However, we do allow for density stratification, so we will need to check that the logarithmic gradient of the density is much smaller than the logarithmic gradient of  $v_z$ . A plot comparing the two quantities is presented in Figure 13. We see that the difference is more than an order of magnitude, enough to justify ignoring the density term for the perturbative calculation.

To perform the calculation, we use a discrete Fourier transform to estimate the spectra of the velocities and density needed in Equation (81), but before that, we again re-sample to a grid that has its collocation points evenly spaced in the vertical direction. We have to be careful when using discrete Fourier transforms to estimate spectra. In particular, we need to pay special

attention to the  $z$  and time directions, since they are not periodic and hence the discrete Fourier transforms suffer from windowing effects. To confirm that our results are not significantly affected, we perform the same calculations using no windowing in those two directions, as well as Welch (parabolic) and Bartlett (triangular) windows. Also it is possible that the impenetrable top and bottom walls might influence our result. So we also tried Welch and Bartlett window functions that exclude the top 12.5% and the bottom 5%. Finally, we performed the calculation with two different density scale heights: infinity and the volume-averaged  $H_\rho$ . The resulting effective viscosity scalings from all these tries were within 15% of each other.

Since the turbulent flow is anisotropic we expect that the effective viscosity is anisotropic. This means that the viscosity

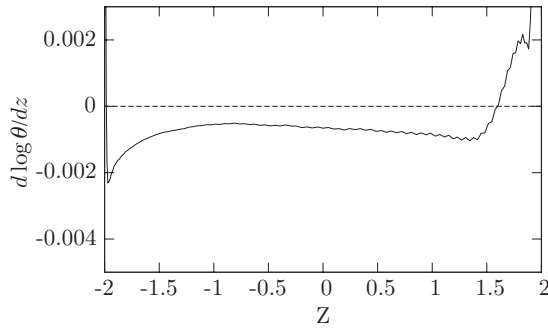


**Figure 12.** Average logarithmic gradient of the potential temperature.

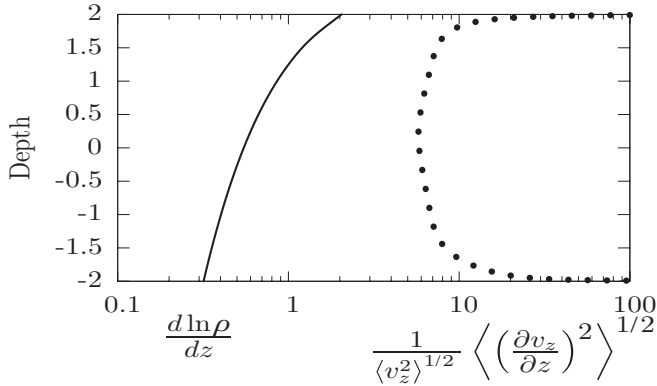


**Figure 13.** Comparison between the logarithmic derivative of the vertical velocity (dashed curve) and the background density (solid curve) for the steady-state flow simulated with our anelastic code.

for us is a rank-four tensor— $K_{ijmn}$ . This tensor must obey a set of symmetries to ensure that the torque on fluid elements is finite. Further, since there is no physical difference between the two horizontal directions, we expect that  $K_{ijmn}$  will be symmetric under rotation/reflection around the vertical axis. After all these symmetries are taken into account, many components of  $K_{ijmn}$  are shown to be zero and the rest can be expressed in terms of five independent quantities (see Penev et al. 2009b, Section 2.2)— $K_0$ ,  $K_0'$ ,  $K_{00'}$ ,  $K_1$ , and  $K_2$ —as follows:

$$\begin{aligned} K_0 &= \frac{1}{2} (K_{1111} + K_{1122}) \\ K_0' &= K_{3333} \\ K_{00'} &= K_{1133} \\ K_1 &= K_{1313} \\ K_2 &= \frac{1}{2} (K_{1111} - K_{1122}). \end{aligned} \quad (82)$$

We can extract the  $K_m$  quantities by comparing the energy dissipation rate of Equation (81) to the dissipation that would occur in the presence of actual anisotropic viscosity:

$$\begin{aligned} \dot{\mathcal{E}}_{\text{visc}}(\Omega) &= \frac{1}{2} \int_0^{L_z} dz [4K_1 |\mathcal{A}_1|^2 + K_2 |\mathcal{A}_2|^2 + K_0 \mathcal{A}_0^2 \\ &\quad + K_0' \mathcal{A}_0'^2 + 2K_{00'} \mathcal{A}_0 \mathcal{A}_0']. \end{aligned} \quad (83)$$

Since in Equation (83) we allow the viscosity to depend on depth, and there is no way to constrain this dependence, we have to choose some radial profile a priori. Our choice is motivated by the mixing length theory:

$$K_m(z) = K_m^0(\Omega) \rho \langle v^2 \rangle^{1/2} H_p, \quad (84)$$

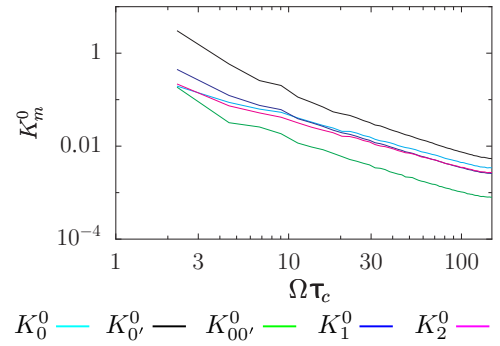


**Figure 14.** Five viscosity parameters as estimated from the steady-state unforced convective flow. The vertical axis is the effective viscosity in units of  $\langle v_z^2 \rangle^{1/2} H_p$  ( $H_p$ : pressure scale height) and the horizontal axis is the perturbation frequency in units of inverse convective turnover times ( $\tau_c$ ).

(A color version of this figure is available in the online journal.)

where  $K_m^0$  are dimensionless constants, that depend on the frequency of the external shear ( $\Omega$ ), and  $H_p$  is the local pressure scale height. This is a sensible choice, since the turbulent viscosity should scale as the length scale and the velocity scale of the problem. Clearly, the velocity scale is that of convection, and in the spirit of mixing length theory, we use the pressure scale height as the length scale. If the mixing length paradigm is relevant, we expect that the value of  $K_m^0$  should scale as the mixing length parameter for the particular simulation.

The resulting frequency dependencies of the five viscosity parameters are presented in Figure 14. As we can see, all terms have similar scaling with frequency, and the relative magnitudes of the distinct components obey the same relations as the Penev et al. (2009b) viscosity calculated for realistic models of the surface convection of low-mass stars.

The approximate period dependence of the viscosity components we find is

$$\begin{aligned} K_m &= \mathcal{K}_m^0 \rho \langle v^2 \rangle^{1/2} H_p \left( \frac{T}{\tau_c} \right)^\lambda, \quad m \in \{0, 0', 00', 1, 2\} \\ \lambda &= 1.05 \pm 0.1, \\ \mathcal{K}_0 &= 0.068 \pm 0.01, \\ \mathcal{K}_{0'} &= 0.18 \pm 0.02, \\ \mathcal{K}_{00'} &= 0.019 \pm 0.005, \\ \mathcal{K}_1 &= 0.066 \pm 0.01, \\ \mathcal{K}_2 &= 0.05 \pm 0.01, \end{aligned} \quad (85)$$

where  $T \equiv 2\pi/\Omega$  and the errors quoted correspond to the range of values encountered for the different window functions and density scale heights.

## 6. CONCLUSION

The above result points to the possibility that viscosity in turbulent convection zones loses efficiency significantly slower than what Kolmogorov scaling predicts at least on large timescales. This seems to be due to the fact that the turbulent eddies with turnover times similar to these large timescales are not in the inertial subrange and hence, the velocity power spectrum is much shallower than the Kolmogorov 5/3 law. This result is not conclusive, since the possibility remains that dropping higher order terms in the above expansion is not a good approximation.

In Penev et al. (2009a), we introduce horizontal depth dependent forcing into the flow equations and obtain the dissipation

properties of the turbulent convective flow directly. We were then able to compare the average rate of work done on the flow by the external forcing to the expected rate of energy transport and dissipation by an assumed effective viscosity. We found that with sufficiently long-time average these two quantities have the same depth dependence, thus verifying the validity of the assumption that an effective viscosity coefficient is sufficient to parameterize the average dissipation and momentum transport properties of the turbulent convective flow for large spatial scales. Further, by repeating the above procedure a number of times we were able to derive the scaling of this effective viscosity coefficient with period and confirm that it is linear.

In this paper, we presented a code that is well suited for the purpose of studying turbulent dissipation in convective zones. First, it is a spectral code, which means that the spatial accuracy is exponential, and hence the code is able to reliably simulate turbulent flows at modest resolutions. Further, by using the anelastic approximation, we do not need to deal with sound waves and shocks. This allows us to take much larger time steps (by more than an order of magnitude) than with a fully compressible code, and hence we can have runs that cover a much longer physical time than fully compressible simulations. This is important, since the external forcing regimes we are interested in are tides with orbital periods of several days, which is not achievable in reasonable time with fully compressible codes.

The price we pay of course is that the flow we simulate is not a good approximation to the flow in any star's surface convection zone. First, we cannot accommodate the region where the driving of the convection occurs, because this region is characterized by strongly supersonic flows and shocks. Also the photon mean free path in that region is not small so the radiative effects can no longer be captured by a heat diffusion coefficient. Second, our code uses the ideal gas equation of state which is a poor approximation to the upper layers of stars. Finally, we do not consider either rotation or magnetic fields, both of which might have an important effect on the dissipative efficiency of the convective zone.

However, the scaling of the effective viscosity with frequency we obtained (Equation (85)) for our box is linear just as the scaling obtained with the same perturbative approach applied to realistic simulations of the upper layers of the convection zones of the Sun and two smaller stars (Penev et al. 2009b). The effective viscosity of Equation (85) is a bit more than two times larger than the effective viscosities from the realistic stellar models, but this is expected, since the mixing length parameter for our box is about two times larger than for those simulations, and as we noted before, we expect that the effective viscosity should be proportional to the mixing length parameter. This gives us confidence that our results are applicable to the systems we are interested in studying.

### 6.1. Comparing to Other Codes

There are a large number of other anelastic numerical codes aiming to study convection in stars or giant planets (Lantz & Fan 1999; Glatzmaier 1984; Jones & Kuzanyan 2009, etc.), the ASH code (Miesch et al. 2000; Elliott et al. 2000; Tobias et al. 2001; Brun & Toomre 2002; Miesch et al. 2008; Brown et al. 2010; Featherstone et al. 2009; among many others). Each of these groups has made different design decisions for the numerical scheme they implement, mostly dictated by the problems the particular numerical code was designed to study.

Here we compare the design decisions we have made to those of the above authors.

Two major differences between the code presented in this paper and (some) of these other codes are that they consider spherical shells encompassing the entire star/planet in some radius range, while we consider only a small region in which we ignore the spherical geometry and approximate it as plane-parallel, and that we ignore magnetic fields. Thus we apply the fast, albeit less detailed evolution typically used to study convective zones globally to a small localized rectangular box, usually treated fully compressibly (e.g., Chan & Sofia 1989, 1996; Cattaneo et al. 1991; Kim et al. 1995; Stein et al. 1989; Robinson et al. 2003, etc.), allowing us to simulate a well-resolved local flow over a long-time period, which is necessary for our purposes.

In addition, as stated in Section 2, instead of using the appropriate expansion in perturbed quantities for the ideal gas equation of state we modify the expression in order to obtain a set of equations which preserve energy exactly instead of only to lowest order in perturbed quantities.

Also, unlike the ASH code, for example, we consider our background variables constant in time, which simplifies the evolution equations considerably, and unlike many anelastic codes we evolve the actual velocity and potential temperature rather than conserved quantities such as vorticity, momentum, energy, and poloidal/toroidal velocity fields.

And finally, our treatment of the subgrid dissipation is markedly different from all other anelastic codes in that we do not introduce actual viscosity (assumed to be due to unresolved turbulent cascade), but rather keep the numerical integration stable by the hyperviscosity discussed in Section 3.2.2, which only affects the simulated flow on scales a few times larger than the grid resolution.

We acknowledge the contribution of Philip Marcus to the development of the original code (Barranco & Marcus 2006).

## APPENDIX A

### IMPLEMENTING THE PRESSURE STEP

As discussed in Section 3.2.3 in order to advance the enthalpy by one time step we need to solve the following differential equation/boundary conditions problem:

$$\left[ \nabla^2 + \frac{d \log \bar{\rho}}{dz} \frac{\partial}{\partial z} \right] \Pi^{N+1} = \frac{1}{\Delta t} \left( \nabla \cdot \mathbf{v}^{N+\frac{2}{3}} + v_z^{N+\frac{2}{3}} \frac{d \log \bar{\rho}}{dz} \right) \\ \frac{\partial \Pi^{N+1}}{\partial z} \Big|_{\pm L_z/2} = \frac{1}{\Delta t} v_z^{N+\frac{2}{3}} \Big|_{\pm L_z/2}. \quad (\text{A1})$$

The solution is obtained in two steps: first, we impose the boundary conditions by ignoring the differential equation for the two highest Chebyshev modes and replacing it with the equations for the boundary conditions; then we use a Green's step (see Appendix A.1) to fix the equation for those two highest modes and instead impose the boundary conditions at the expense of ignoring the momentum Equation (19) at the two highest modes.

We need to solve Equation (A1) as efficiently as possible. Clearly, we can make this a trivial matrix multiplication operation if we were to store the inverse of the left-hand side operator for each horizontal mode at the start, and at each time step we multiply every vertical slice of the transformed right-hand side

by the corresponding inverse to get the value of  $\Pi^{N+1}$ . However, this would require  $N_x \times N_y$  matrices of  $N_z^2$  elements to be stored (where  $N_x$ ,  $N_y$ , and  $N_z$  are the resolutions in the  $\hat{x}$ ,  $\hat{y}$ , and  $\hat{z}$  directions, respectively), which for large resolutions is likely to exceed the amount of memory available on each node of the cluster where the code is to run.

To avoid this, we need to find the most efficient approach that only stores things common to all horizontal modes. We see that the pressure equation is almost identical for all horizontal modes, except for the horizontal component of the  $\nabla^2$  operator, which in Fourier space means simply multiplying by  $k_\perp^2 \equiv k_x^2 + k_y^2$ , where  $k_x$  and  $k_y$  are the corresponding  $\hat{x}$  and  $\hat{y}$  wavenumbers for each mode. So what we can reasonably do is to pre-compute the common part of the left-hand side operator, and then for each horizontal mode add  $k_\perp^2$  along the diagonal. We then overwrite the last two rows of the resulting matrix ( $\mathbf{M}_{i,j}$ ) with

$$M_{N_z,p} = p^2, \quad (\text{A2})$$

$$M_{N_z-1,p} = (-1)^p p^2, \quad (\text{A3})$$

in order to impose the boundary conditions, decompose  $\mathbf{M}$  into upper and lower triangular parts, and solve by backward substitution. The right-hand side vector also needs to have its highest two entries overwritten with the boundary conditions at the top and bottom of the box, respectively.

### A.1. Green's Step

In this step, we fix the anelastic constraint even for the two highest Chebyshev modes, and instead break the two highest modes of the momentum equation (19) to satisfy the boundary conditions which we break in the process. To make the expressions shorter, define the following operators:

$$D \equiv \frac{d}{dz}, \quad (\text{A4})$$

$$D_A \equiv \frac{d}{dz} + \frac{d \ln \bar{\rho}}{dz}, \quad (\text{A5})$$

$$\nabla \equiv ik_x \hat{x} + ik_y \hat{y} + D \hat{z}, \quad (\text{A6})$$

$$\nabla_A \equiv ik_x \hat{x} + ik_y \hat{y} + D_A \hat{z}, \quad (\text{A7})$$

$$\Delta_A \equiv \nabla_A \cdot \nabla. \quad (\text{A8})$$

We would like to modify the pressure step in a way that will include two new degrees of freedom, which we can then use to fix the anelastic constraint for the two highest Chebyshev modes. The particular modification useful in this case is

$$\mathbf{v}^{N+1} = \mathbf{v}^{N+\frac{2}{3}} - \Delta t \nabla \Pi^{N+1} + \hat{z} (\tau_1^{N+1} T_{N_z-1} + \tau_2^{N+1} T_{N_z}), \quad (\text{A9})$$

where  $T_N$  denotes a Chebyshev polynomial of order  $N$ ,  $\tau_1$  and  $\tau_2$  are arbitrary coefficients to be chosen later,  $N_z$  is the order of the highest Chebyshev coefficient we are simulating, and the superscripts refer to the time index, with non-integer values corresponding to fractional steps.

Requiring the anelastic constraint and velocity boundary conditions gives

$$\Delta_A \Pi^{N+1} = \frac{1}{\Delta t} \nabla_A \cdot \mathbf{v}^{N+\frac{2}{3}} + \tau_1^{N+1} D_A T_{N_z-1} + \tau_2^{N+1} D_A T_{N_z}, \quad (\text{A10})$$

$$D \Pi^{N+1} |_{\pm L_z/2} = \frac{1}{\Delta t} v_z^{N+\frac{2}{3}} + \tau_1^{N+1} T_{N_z-1} + \tau_2^{N+1} T_{N_z} \Big|_{\pm L_z/2}. \quad (\text{A11})$$

To proceed we break up  $\Pi^{N+1}$  into three pieces:

$$\Pi^{N+1} = \Pi_0^{N+1} + \frac{1}{\Delta t} (\tau_1^{N+1} \Gamma_1^{N+1} + \tau_2^{N+1} \Gamma_2^{N+1}). \quad (\text{A12})$$

This allows us to split the above equation into three separate equations with corresponding boundary conditions, the first of which is the already calculated pressure step:

$$\Delta_A \Pi_0^{N+1} = \frac{1}{\Delta t} \nabla_A \cdot \mathbf{v}^{N+\frac{2}{3}}, \quad (\text{A13})$$

$$D \Pi_0^{N+1} |_{\pm L_z/2} = \frac{1}{\Delta t} v_z^{N+\frac{2}{3}} \Big|_{\pm L_z/2}, \quad (\text{A14})$$

$$\Delta_A \Gamma_1^{N+1} = D_A T_{N_z-1}, \quad (\text{A15})$$

$$D \Gamma_1^{N+1} |_{\pm L_z/2} = T_{N_z-1} |_{\pm L_z/2}, \quad (\text{A16})$$

$$\Delta_A \Gamma_2^{N+1} = D_A T_{N_z}, \quad (\text{A17})$$

$$D \Gamma_2^{N+1} |_{\pm L_z/2} = T_{N_z} |_{\pm L_z/2}. \quad (\text{A18})$$

We solve the two new equations in the same way we solve the first one. This makes as before the anelastic constraint satisfied for all but the two highest Chebyshev modes, but this time we have two arbitrary constants  $\tau_1$  and  $\tau_2$  which we can then set to values that will make the anelastic constraint hold for those two modes as well.

## APPENDIX B

### IMPLEMENTING THE HEAT DIFFUSION STEP

The same considerations as the pressure step apply to this step. We again decide against making a table of pre-inverted matrices for each horizontal mode, and instead we only pre-compute the part of the matrix that is common for all horizontal modes. To make the description of the numerical procedure followed clearer, we define the following matrices:

- $CP$  : transforms a vector from Chebyshev to physical space
- $PC = CP^{-1}$  : transforms a vector from physical to Chebyshev space
- $D$  : differentiates a vector in Chebyshev space.

From those we construct a derivative operator and the common part of the left-hand side operator, both in physical space:

$$D_P \equiv CP \cdot D \cdot PC, \quad (\text{B1})$$

$$M_P \equiv D_P \cdot D_P + F \cdot D_P + G, \quad (\text{B2})$$

where  $F$  and  $G$  are diagonal matrices defined by

$$F_{ij} \equiv C_1(z_i)\delta_{ij}, \quad (\text{B3})$$

$$G_{ij} \equiv (C_2(z_i) + C_3(z_i))\delta_{ij}, \quad (\text{B4})$$

with  $z_i$  being the  $i$ th vertical collocation point as defined in Equation (31), and  $C_1$  and  $C_2$  are given by Equations (48) and (49), respectively.

What we pre-compute and store is a matrix  $\mathbf{M}$ , which we obtain by overwriting the first and last rows of  $M_P$  with

$$M_{P1,1} = 1 \quad M_{P1,j} = 0, \quad j = 2 \dots N_z, \quad (\text{B5})$$

$$M_{PN_z,j} = 0, \quad j = 1 \dots N_z - 1 \quad M_{PN_z,N_z} = 1, \quad (\text{B6})$$

to allow for imposing the boundary conditions, then sandwiching the resulting matrix between  $PC$  and  $CP$ :

$$\mathbf{M} \equiv PC \cdot M_P \cdot CP. \quad (\text{B7})$$

For each time step, in order to solve Equations (52) and (53) for each horizontal mode we construct a new matrix  $\mathbf{M}'(k_\perp)$  from  $\mathbf{M}$  as follows:

$$\begin{aligned} \mathbf{M}'_{i,j}(k_\perp) \equiv & \mathbf{M}_{i,j} - k_\perp^2 \delta_{i,j} + k_\perp^2 (PC_{i,0}CP_{0,j} \\ & + PC_{i,N_z-1}CP_{N_z-1,j}). \end{aligned} \quad (\text{B8})$$

The first new term adds the horizontal part of the  $\nabla^2$  operator for the given mode, however, this breaks the requirements for the boundary conditions, so we repair them with the other two terms. This way, the boundary conditions are directly imposed by breaking Equation (52) at the physical top and bottom of the box, instead of ignoring it for the two highest Chebyshev modes. That means we do not need to perform extra Green's steps like we did for the pressure equation. We obtain the solution to Equation (52) by decomposing  $\mathbf{M}'(k_\perp)$  into upper and lower triangular matrices and using back-substitution.

## REFERENCES

- Bannon, P. R. 1996, *J. Atmos. Sci.*, **53**, 3618  
 Barranco, J. A., & Marcus, P. S. 2006, *J. Comput. Phys.*, **219**, 21  
 Boyd, J. 1998, *J. Comput. Phys.*, **143**, 283  
 Brown, B. P., Browning, M. K., Brun, A. S., Miesch, M. S., & Toomre, J. 2010, *ApJ*, **711**, 424  
 Brun, A. S., & Toomre, J. 2002, *ApJ*, **570**, 865  
 Cattaneo, F., Brummell, N. H., Toomre, J., Malagoli, A., & Hurlburt, N. E. 1991, *ApJ*, **370**, 282  
 Chan, K. L., & Sofia, S. 1989, *ApJ*, **336**, 1022  
 Chan, K. L., & Sofia, S. 1996, *ApJ*, **466**, 372  
 Clune, T., Elliott, J. R., Glatzmaier, G. A., Miesch, M. S., & Toomre, J. 1999, *Parallel Comput.*, **25**, 361  
 Elliott, J. R., Miesch, M. S., & Toomre, J. 2000, *ApJ*, **533**, 546  
 Featherstone, N. A., Browning, M. K., Brun, A. S., & Toomre, J. 2009, *ApJ*, **705**, 1000  
 Glatzmaier, G. A. 1984, *J. Comput. Phys.*, **55**, 461  
 Goldreich, P., & Keeley, D. A. 1977, *ApJ*, **211**, 934  
 Goldreich, P., & Kumar, P. 1988, *ApJ*, **326**, 462  
 Goldreich, P., Murray, N., & Kumar, P. 1994, *ApJ*, **424**, 466  
 Goldreich, P., & Nicholson, P. D. 1977, *Icarus*, **30**, 301  
 Gonczi, G. 1982, *A&A*, **110**, 1  
 Goodman, J., & Oh, S. P. 1997, *ApJ*, **486**, 403  
 Jones, C. A., & Kuzanyan, K. M. 2009, *Icarus*, **204**, 227  
 Kim, Y., Fox, P. A., Sofia, S., & Demarque, P. 1995, *ApJ*, **442**, 422  
 Lantz, S. R., & Fan, Y. 1999, *ApJS*, **121**, 247  
 Malagoli, A., Cattaneo, F., & Brummell, N. H. 1990, *ApJ*, **361**, L33  
 Meibom, S., & Mathieu, R. D. 2005, *ApJ*, **620**, 970  
 Miesch, M. S., Brun, A. S., De Rosa, M. L., & Toomre, J. 2008, *ApJ*, **673**, 557  
 Miesch, M. S., Elliott, J. R., Toomre, J., Clune, T. L., Glatzmaier, G. A., & Gilman, P. A. 2000, *ApJ*, **532**, 593  
 Penev, K., Barranco, J., & Sasselov, D. 2009a, *ApJ*, **705**, 285  
 Penev, K., Sasselov, D., Robinson, F., & Demarque, P. 2009b, *ApJ*, **704**, 930  
 Porter, D. H., & Woodward, P. R. 2000, *ApJS*, **127**, 159  
 Robinson, F. J., Demarque, P., Li, L. H., Sofia, S., Kim, Y.-C., Chan, K. L., & Guenther, D. B. 2003, *MNRAS*, **340**, 923  
 Sofia, S., & Chan, K. L. 1984, *ApJ*, **282**, 550  
 Stein, R. F., & Nordlund, A. 1989, *ApJ*, **342**, L95  
 Stein, R. F., Nordlund, A., & Kuhn, J. R. 1989, in *Solar and Stellar Granulation*, ed. R. J. Rutten & G. Severino (Dordrecht: Kluwer), 381  
 Tobias, S. M., Brummell, N. H., Clune, T. L., & Toomre, J. 2001, *ApJ*, **549**, 1183  
 Verbunt, F., & Phinney, E. S. 1995, *A&A*, **296**, 709  
 Zahn, J. P. 1966, *Ann. Astrophys.*, **29**, 489  
 Zahn, J. P. 1989, *A&A*, **220**, 112